

Fast Full-wave Electromagnetic Inverse Scattering Based on Scalable Cascaded Convolutional Neural Networks

Kuiwen Xu, *Member, IEEE*, Chen Zhang, Xiuzhu Ye, and Rencheng Song, *Member, IEEE*,

Abstract—The end-to-end scalable cascaded convolutional neural networks (SC-CNNs) are proposed to solve inverse scattering problems (ISPs) and the high-resolution image can be directly obtained from the scattered field with the guiding by multi-resolution labels in the cascaded blocks. To alleviate the difficulty of solving the ISPs via a full-wave way, the proposed SC-CNNs are physically decomposed into two parts, i.e., the linear transformation and the multi-resolution imaging networks. The first part is composed of one CNN block and is used to mimic the linear transformation (e.g., back propagation, BP) from scattered field to the preliminary image. Whereas, the second part consists of a few cascaded CNN blocks to realize the reconstruction from the rough image to high-resolution image. With more high-frequency components incorporating into the multi-resolution labels, the cascaded networks can be guided through those labels, avoiding black-box operations and enhancing the physical meaning and interpretability. The proposed SC-CNNs are verified by both the synthetic and experimental examples and it is proven that better performance can be achieved in terms of both inversion accuracy and efficiency compared to the BP-Unet and direct inversion scheme (DIS).

Index Terms—End-to-end, full-wave inversion, scalable cascaded convolutional neural networks (SC-CNNs), multi-resolution label.

I. INTRODUCTION

INVERSE scattering problems (ISPs) are a type of quantitative microwave imaging method, which is essentially to obtain the size, position, shape and constitutive parameters, such as the relative permittivity and the conductivity, by use of the measured scattered field. It is now widely reported in various fields, such as through-wall imaging [1], [2], remote sensing [3], bio-medical imaging [4] and so on [5], [6]. Whereas, owing to the inherent multiple scattering and the

limit measurement data, there are still two major challenges in ISPs: nonlinearity and ill-posedness. Consequently, lots of reconstruction methods have been proposed to alleviate these two problems according to the physical models.

Reconstruction methods can be classified into iterative methods and non-iterative methods. Subspace optimization method (SOM) [7]–[9], contrast source inversion method (CSI) [10]–[12], distorted Born iterative method (DBIM) [13], and some other Newton typed methods [14], [15] are classical iterative nonlinear optimization methods. Although these methods have strong capability to solve the ISPs in a wide range of applications, they are still time-consuming, especially for the three-dimensional (3-D) ISPs. Non-iterative methods contain Born approximation inversion method [16], the back propagation (BP) method [17], linear sampling method (LSM) [18], direct sampling method (DSM) [19], etc. These methods transform nonlinear problems into some linear problems based on the Born approximation, which can reduce the computational cost and source due to high computational complexity. But the results obtained from non-iterative approaches usually result in the failure reconstruction especially for the strong scatterers (those with high contrast and electrically large dimension). Therefore, traditional inversion methods are hard to meet the requirement on both the reconstruction accuracy and the real-time implementation.

In order to tradeoff the computational cost and the reconstruction accuracy, some machine learning-based inversion methods are presented [20], [21]. Inspired by the powerful representation capabilities of deep neural networks (DNN) [22], the neural networks are used to build a nonlinear mapping between the scattered field and the unknown constitutive parameters of scatterers. And the deep learning-based inversion methods can be generally divided into two categories. One is using neural networks to fulfill the image-to-image mapping, in which the input images can be obtained from some non-iterative fast methods [23]–[25]. These non-iterative approaches are used to transform the measured scattered field into coarse profiles along with low-frequency components and extract prior physical information in advance. The purpose of the neural networks is to restore the high-frequency components of the profile with the aid of the rough input profile, which significantly reduces the afford of the networks in direct inversion scheme (DIS) [24] with the input of the scattered field. However, the inversion accuracy of these methods are highly depending on the quality of input images. If the input image is close to the reference one, it is expected to get

Manuscript received xxx; revised xxx. This work was supported by the China Postdoctoral Science Foundation under Grant 2019M661984, the Zhejiang Provincial Natural Science Foundation of China under Grant LY19F010012, the National Natural Science Foundation of China under Grant 61971174, and in part by the Talent Project of Zhejiang Association for Science and Technology under Grant SKX201901. (Corresponding author: Rencheng Song)

K. Xu is with Engineering Research Center of Smart Microsensors and Microsystems, Ministry of Education, Hangzhou Dianzi University, Hangzhou China and also with School of Mechatronic Engineering, China University of Mining and Technology, Xuzhou, Jiangsu, China (e-mail: kuiwenxu@hdu.edu.cn).

C. Zhang is with Engineering Research Center of Smart Microsensors and Microsystems, Ministry of Education, Hangzhou Dianzi University, Hangzhou 310018, China.

X. Ye is with the Beijing Institute of Technology, Beijing 10081, China (e-mail: xiuzhuye@outlook.com)

R. Song is with the Department of Biomedical Engineering, Hefei University of Technology, Hefei 230009, China (email: rcsong@hfut.edu.cn).

good reconstruction. Otherwise, if the mapping between the rough input and the reference image is quite complicated, it may distort the results and the generalization capability of the deep model. The other type aims to replace some key operators (usually with the large amount of computations) in nonlinear iterative methods with the trained neural networks to accelerate the inversion. For example, in [27], they use deep neural network (DNN) to train the most time-consuming gradient, rather than retrieving high-resolution image directly. The full inversion is still following an iterative framework and has better generalization capability compared to the first type methods. But the computational cost is usually high, especially for 3-D ISPs, since the method is still iterative.

Although the results of existing machine learning-based inversion are encouraging, researchers also have tried efforts to achieve end-to-end approaches [24], [28], in which the neural network is taken to directly build a mapping between input and output profiles. In virtue of one cost function in the network, the problem can be solved in one step and the computational complexity is also reduced to some extent. However, most of the end-to-end networks are like a black-box method, in which the contribution of each part is unknown. And the underlying wave physics is almost lost such that the generalization ability is weakened significantly. For example, DIS mentioned in [24] can only reconstruct some simple scatterers in the range of training set and edges of the reconstructed profiles are blurred.

To alleviate this problem, in [29], the mapping from the scattered field to the targets is directly divided into two steps, i.e., the first step is to get a rough input and the second step is to obtain a high-resolution image (e.g, high-resolution herein is compared to the results got by BP) and the labels for two networks are the ground truth. The physical insight is not well embodied in the network. Inspired by the cascaded CNN in [30], in this paper, multi-resolution labels in the scalable cascaded convolutional neural networks (SC-CNNs) are used to gradually guide the inversion. Different from the work of implementing the induced current mapping in [30], a direct inversion from the scattered field to the images in one step is achieved by the proposed SC-CNNs. With the cascaded networks, the entire physical model is established step by step and by the guiding of the intermediate labels and the network is made more easily to learn the underlying relationship between labels. And the contribution of each block is controlled by the corresponding weight coefficient in the loss functions.

The cascaded network mainly contains two parts. The first part of the network is to realize the mapping of the scattered field to a rough intermediate image (such as the results of the BP), and the second part gradually realizes the process from the rough intermediate image to final high-resolution image. More and more high-frequency components are retrieved by the cascaded network in the second part. Herein, the cost function is a sum of the weighted pixel-wise mean squared error (MSE) and the multi-resolution labels are used to guide the image reconstruction process. In the inversion, the results of BP are taken as the first intermediate label considering that the mapping between the scattered field and the BP image is linear which is easy to be approximated through

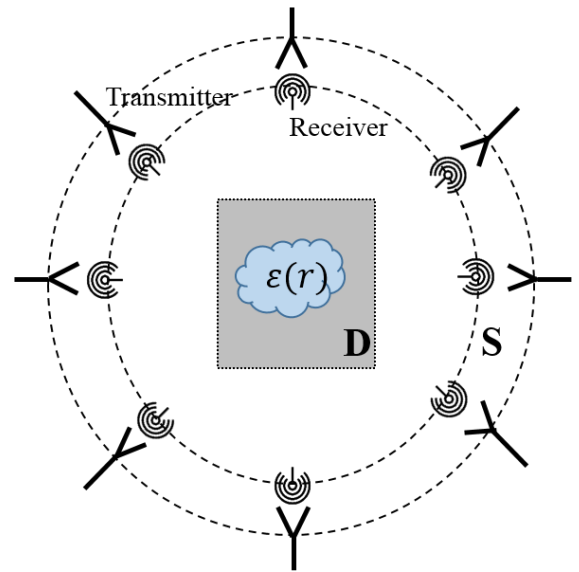


Fig. 1. Schematic diagram of inverse scattering problems.

neural networks. Consequently, the proposed method converts a complicated nonlinear mapping into a composite of a several simple mappings, through the use of multi-label learning, which not only reduces the difficulty of training, but also enhances the physical meaning and interpretability of the network. The contributions of this paper are summarized as follows:

1. The end-to-end scalable cascaded convolutional neural networks (SC-CNNs) are proposed to build a mapping between the scattered field and the final output image. Multiple-resolution labels are used to guide the reconstruction process. The proposed SC-CNNs restrict the physical meaning of the hidden layers of the network, which is explicitly constrained as that the characteristics that the network needs to learn. Specifically, the result of BP is taken as the label of the first block of neural network such that it can well learn the linear relationship between the label and the scattered field. Later, with more high-frequency components incorporating into the multi-resolution labels, the guiding of cascaded network can avoid black-box operations and enhance the physical meaning and interpretability of the neural network. The high-resolution reconstruction image and better generalization ability can be finally achieved.

2. The proposed approach can achieve better performance in terms of the accuracy and efficiency compared to both of the direct inversion scheme (DIS) and the BP-Unet in [24], [26].

3. According to the difficulties of the problems to be solved, the second part of the SC-CNNs can be scaled and we can add or reduce the corresponding number of blocks according to the complexity of the imaging targets, thereby obtaining better results than the existing BP-Unet.

The structure of this paper is arranged as follows: in Section II, formulation of the problem is presented. In Section III, the cascaded network is proposed, including its structure and label generation. We show the test results of numerical and experimental data in Section IV, and at last, in Section V, we

will give a summary of this paper.

It is worth noting that we use \bar{X} and \bar{X} to represent the matrix and vector of the discretized operator or parameter X , respectively. The superscripts H and * respectively means conjugate transpose and complex conjugate of a matrix or vector.

II. FORMULATION OF THE PROBLEM

Herein, a two-dimensional (2-D) ISPs with transverse-magnetic (TM) polarization with time harmonic fields of $e^{(-i\omega t)}$ (ω is the angular frequency) is considered. We illustrate the problem with a 2-D example. The configuration of 2-D ISPs is shown in Fig. 1, in which the scatterers are located at the domain of interest (DoI) D in a homogeneous background. The permittivity, permeability, and wavenumber of the homogeneous background are denoted as ε_0 , μ_0 , and $k_0 = \omega\sqrt{\mu_0\varepsilon_0}$, respectively. There are N_i incident antennas and N_r receiving antennas uniformly distributed around the scatterers. The incident antennas are located at \mathbf{r}_p^i with $p = 1, 2, \dots, N_i$, and they transmit the electromagnetic signals in turn. And at the same time, all the receivers, located at \mathbf{r}_p^s with $q = 1, 2, \dots, N_r$ on the measurement domain S , collect scattered field data together [31].

In the forward problem, it is to get the scattered field for the known scatterers and the given incident fields. The inverse problems are to reconstruct the constitutive parameters of the unknown targets given a set of $N_r \times N_i$ scattering data. It is well known, the Lippmann-Schwinger integral equation describes the interaction of the scattering behavior, in the following, the 2-D integral equations are used to build the formulas. The total fields in the DoI can be calculated by,

$$E_p^{tot}(\mathbf{r}) = E_p^{inc}(\mathbf{r}) + k_0^2 \int_D G(\mathbf{r}, \mathbf{r}') I_p(\mathbf{r}') d\mathbf{r}' \quad \mathbf{r} \in D \quad (1)$$

where $E_p^{tot}(\mathbf{r})$ and $E_p^{inc}(\mathbf{r})$ are the total electric field and incident electric field at \mathbf{r} , respectively and \mathbf{r}' denotes the position of a source point. $G(\mathbf{r}, \mathbf{r}') = \frac{i}{4} H_0^1(k_0 |\mathbf{r} - \mathbf{r}'|)$ represents the 2-D Greens function in free space, where $H_0^1(k_0 |\mathbf{r} - \mathbf{r}'|)$ is the first-kind zeroth-order Hankel function. $I_p(\mathbf{r}')$ denotes the contrast current source, which can be defined as,

$$I_p(\mathbf{r}') = \frac{J_p(\mathbf{r}')}{-i\omega\varepsilon_0} = \chi(\mathbf{r}') E_p^{tot}(\mathbf{r}') \quad \mathbf{r}' \in D \quad (2)$$

where $J_p(\mathbf{r}')$ denotes as the physical induced current and the contrast function can be written as $\chi(\mathbf{r}') = \varepsilon_r(\mathbf{r}') - 1$. The Eq. (1) is considered as the object equation.

The second equation is data equation, which is used to derive the scattered field $E_p^{sca}(\mathbf{r})$ on the domain S , and it is described as,

$$E_p^{sca}(\mathbf{r}) = k_0^2 \int_D G(\mathbf{r}, \mathbf{r}') I_p(\mathbf{r}') d\mathbf{r}' \quad \mathbf{r} \in S \quad (3)$$

In order to numerically solve ISPs, we use the method of moment (MOM) with the pulse basis function and the delta testing function to discretize the DoI D into $M = M_1 \times M_2$ rectangle subunits [32], and the centers of them are located at $\mathbf{r}_1, \mathbf{r}_2, \dots, \mathbf{r}_M$. The discretized formulas of object and data equations are expressed as follows:

$$\bar{E}_p^{tot} = \bar{E}_p^{inc} + \bar{G}_D \cdot \bar{I}_p \quad (4)$$

and

$$\bar{E}_p^{sca} = \bar{G}_S \cdot \bar{I}_p \quad (5)$$

The inverse problem herein is to obtain the constitutive parameters of unknown scatterers, i.e., χ with the scattered field \bar{E}_p^{sca} on the measurement domain S and the corresponding illumination fields according to Eqs. (4) and (5). It can be viewed as a model-based optimization problem, and if we define Ψ as the operator of solving forward problem, i.e., $\bar{E}_p^{sca} = \Psi(\chi)$, the cost function of the ISPs can be expressed as [31],

$$\min : f(\chi) = \sum_{p=1}^{N_i} \|\Psi(\chi) - \bar{E}_{p,mea}^{sca}\|^2 + \alpha R(\chi) \quad (6)$$

where $\bar{E}_{p,mea}^{sca}$ is the measured scattered field data at the p th incidence, $R(\chi)$ is a regularization term to restrict the unknown parameters with some prior information and makes the solution more stable and α is a weighting parameter to balance the data fitting term and the regularization term. Owing to small amount of measurement data and noise, the above problems counter serious nonlinearity and ill-posedness. BP-Unet mentioned in [24] is to solve the problems. The whole method is divided into two steps, firstly, it obtains an initial image through BP, and then the rough image is taken as the input of the Unet-CNN network to get high-resolution image. Although this approach can achieve good reconstructions, it depends a lot on the initial rough image. Consequently, to solve the problem of relying on the initial image and to simplify the imaging procedure, a new end-to-end method is proposed in the following.

III. SCALABLE CASCADED CONVOLUTIONAL NEURAL NETWORKS

In this paper, end-to-end scalable cascaded convolutional neural networks (SC-CNNs) are proposed to directly get the contrast function from the measured scattered field, e.g., E_p^{sca} . The configuration of this cascaded network is depicted in Fig. 2. The network mainly consists of two parts, and the first part consists of only one block (e.g., one piece of Unet-CNN) which is used to realize the linear manipulation from the scattered field E_p^{sca} to a rough image, while the second part is composed of an indeterminate number of blocks to achieve the high-resolution imaging from the rough profiles with low-frequency components to the high-resolution image ε_r' . All blocks are trained together. Supposed that the cascaded network model is denoted as Γ , and the whole process can be described as,

$$\varepsilon_r' = \Gamma_{\Theta}(E_p^{sca}) \quad (7)$$

where Θ denotes the weight parameters of the SC-CNNs.

In order to alleviate the nonlinearity of ISPs, multiple Unet-CNN blocks are cascaded to guide the nonlinear relationship, and each block has its own label. With the processing of the SC-CNNs, more high-frequency components are included in the corresponding labels of the blocks and the final label is the ground truth.

To gradually achieve the representation of nonlinearity owing to multiple scattering effects, the results of some linear

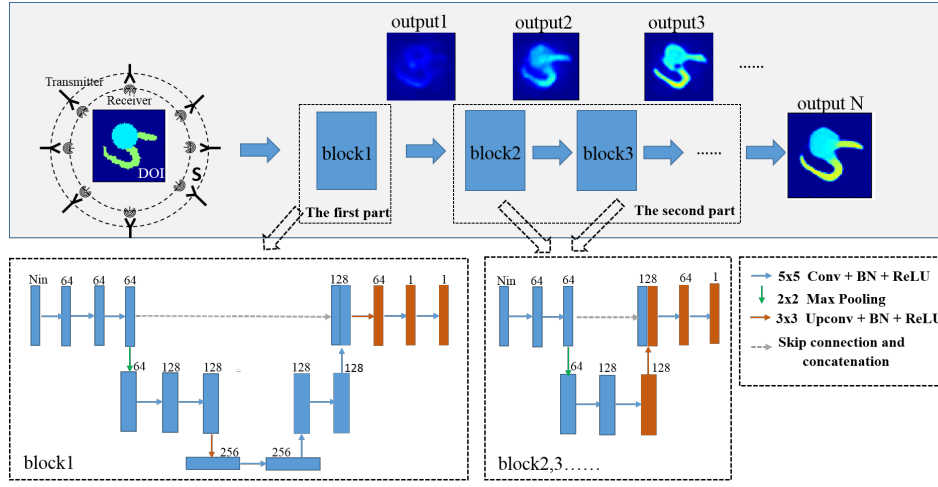


Fig. 2. The proposed end-to-end cascaded network consists of two parts, the first part uses block1 while the second part uses block2, block3, ..., the input is the scattered field generated by MOM and the output is the high-resolution image, output1, output2, output3, ..., output N is the output of each block.

reconstruction methods like BP are taken as the label of block1. Actually, block1 is to fulfill the linear transformation from the scattered field to the preliminary images. In the subsequent networks, block2, block3, ..., are used to improve the image resolution. Block1, block2, block3, ..., mainly refer to simplified the Unet-CNN structure [26]. Although this structure can't perfectly map the scattered field to the ground-truth (i.e. DIS) owing to high nonlinearity of ISPs, it is validated that it can work well in mapping the scattered field to BP image. They mainly contain 5×5 convolution, followed by a batch normalization (BN) [33], a rectified linear unit (ReLU). As for the structure of blocks in the second part, fewer layers are used because several cascaded blocks would be involved to achieve the image-to-image transformation. In the training procedure, all blocks are trained together with a unified weighted cost function. The fulfillment of the blocks and the construction of the SC-CNNs will be described in details in the following subsections.

A. Derivation of BP

Back propagation (BP) is a classical non-iterative inversion method based on Born-approximation, which is a linear method and widely used in the microwave imaging. Here, we use the retrieval profile of this method as the label of the first block. The implementation of BP is divided into three steps. The first step is to calculate induced current $\bar{I} = \gamma \cdot \bar{G}_S^H \cdot \bar{E}^{sca}$ [17], [31]. A cost function F based on Eq. (6) can be defined as,

$$F(\gamma) = \left\| \bar{E}^{sca} - \bar{G}_S \cdot (\gamma \cdot \bar{G}_S^H \cdot \bar{E}^{sca}) \right\|^2 \quad (8)$$

Take the derivative of Eq. (8) with respect to the complex constant γ , and make it equal to 0, and then γ can be got,

$$\gamma = \frac{\left\langle \bar{E}^{sca}, \bar{G}_S \cdot (\bar{G}_S^H \cdot \bar{E}^{sca}) \right\rangle_S}{\left\| \bar{G}_S \cdot (\bar{G}_S^H \cdot \bar{E}^{sca}) \right\|_S} \quad (9)$$

where $\langle A, B \rangle_S$ represents the inner project of the A and B in the domain S. The second step computes the total field in the

domain D by Eq. (4). After that, the contrast $\chi^{BP}(\mathbf{r})$ can be calculated with the least squared method,

$$\chi^{BP}(\mathbf{r}) = \frac{\sum_{p=1}^{N_i} \bar{I}_p(\mathbf{r}) \cdot [\bar{E}_p^{tot}(\mathbf{r})]^*}{\sum_{p=1}^{N_i} \|\bar{E}_p^{tot}(\mathbf{r})\|^2} \quad (10)$$

It can be seen from above steps of BP that the process from the scattering field E^{sca} to the contrast χ^{BP} is a linear process. So, we can easily utilize the neural networks to achieve this linear relationship in the first part, which is a significant step in the SC-CNNs. That is to say, by taking the scattered field as the input of a network, the rough image can be calculated with the BP result as the training label. By this operation, several advantages can be summarized as follows:

1. Through the first block to mimic the BP operation, the scattered fields can be transformed into the preliminary images guided by the results of BP in the training. And the physical characteristics (e.g., the low-frequency components) can be reserved by this operation. The remaining high frequency components can be learned by the subsequent blocks guided by the multiple resolution images. Due to multiple-resolution labels, physical information from the scattered field can be fully utilized in the end-to-end training.

2. If the results of BP algorithm are directly used as the input into successive stages, the whole reconstruction process is divided into two steps. Whereas the proposed SC-CNNs achieve end-to-end mapping and make the inversion more efficiently. if the output of BP is not good under the conventional fixed BP process, it may also result in poor reconstruction results for the final predicted results. Whereas an end-to-end training with successive blocks would affect the output of previous blocks, the proposed SC-CNNs can improve the situation and make the inversion more flexible.

After getting the preliminary image by mimicking the BP result with block1, the remaining task is to achieve image-to-image transformation with different labels of various resolution.

B. Derivation of Multiple-resolution Labels

In the whole SC-CNNs, the small Unet-CNN blocks will increase as the degree of nonlinearity increases (or the difficulty of the ISPs). The number of the blocks after block1 depends on the difficulty of the ISPs. The more difficult the problems you solve, the more number of the blocks should be utilized in the SC-CNNs.

The first block of the SC-CNNs is to realize the process of BP. It is noted that, the results (e.g., reconstructed permittivity) by the BP is extremely close to the one in the background, which is used as the label of the block1 in the SC-CNNs. To distinguish the value of the permittivity of the target and the homogeneous background evidently, the images got from BP, e.g., $\varepsilon_r^{BP}(\mathbf{r})$ is processed logarithmically as $\varepsilon_{r,1}(\mathbf{r}) = \log_{10}(\varepsilon_r^{BP'}(\mathbf{r}))$, and $\varepsilon_r^{BP'}(\mathbf{r})$ is formulated as,

$$\varepsilon_r^{BP'}(\mathbf{r}) = \begin{cases} \varepsilon_r^{BP}(\mathbf{r}), & \varepsilon_r^{BP}(\mathbf{r}) \geq 1 \\ 1.0, & \varepsilon_r^{BP}(\mathbf{r}) < 1 \end{cases} \quad (11)$$

Therefore, the label of the first block is $\varepsilon_{r,1}$, while the label of k th block in the second part is obtained by the following equation,

$$\varepsilon_{r,k}(\mathbf{r}) = \bar{F}^H \cdot \left[\bar{M}_S \circ (\bar{F} \cdot (\varepsilon_r(\mathbf{r}) - \varepsilon_r^{BP}(\mathbf{r}))) \right] + \varepsilon_r^{BP}(\mathbf{r}) \quad (12)$$

where \bar{F} represents the Fourier transform matrix, \circ is Hadamard product, \bar{M}_S is a one-zero matrix where the center part (low-frequency components) with the size of $M_k \times M_k$ is one and the rest of it is zero, $\varepsilon_{r,k}$ stands for the label in the k th block, $k = 2, \dots, N$, and N is the total number of blocks. ε_r is the relative permittivity of the training samples. In the process of producing label of the subsequent blocks, M_k gradually increases until \bar{M}_S becomes a matrix of all ones (e.g., $M_k = M$). The label in the last block is the ground truth. The labels (or the M_k) should be carefully designed such that different labels in the various blocks can be well differentiated and more and more high-frequency components are used to constructed the label.

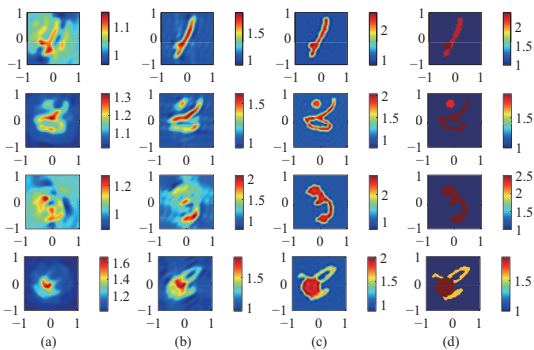


Fig. 3. Four representative examples when four cascaded Unet-CNN blocks are used, with (a) the label of the first block and the result of BP, (b) the label of second block, (c) the label of the third block, (d) the label of the fourth block and ground truth.

As shown in Fig. 3, four examples are used to depict the effects of the multi-resolution labels in the SC-CNNs with four Unet-CNN blocks. It is can be seen clearly that the resolution

of the label is improved as the number of labels increases. And they are getting closer to ground truth. Therefore, besides the first block for transforming the field data to image, the problem is divided into more feasible operators corresponding to the cascaded networks. The highly nonlinear relationship can be achieved by the some gradually cascaded network, which guides network orderly to learn the physical relationship.

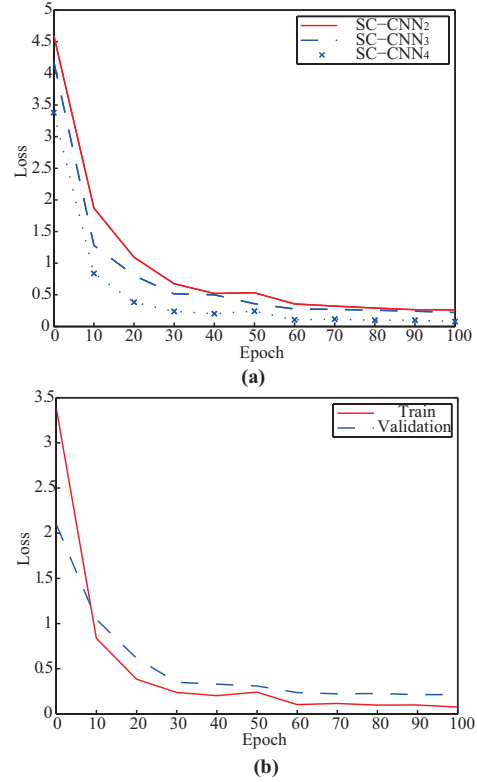


Fig. 4. (a) The convergence curves of the SC-CNN₂, SC-CNN₃, SC-CNN₄ in the training; (b) The loss curves for the training (red line) and validation (blue line) by the SC-CNN₄ with four blocks trained together.

C. Cost Function of SC-CNNs

The SC-CNNs are composed of a series of Unet-CNN blocks. For the convenience of representation, we define k cascaded Unet-CNN blocks as SC-CNN _{k} . For example, if you have four blocks cascaded in the whole SC-CNNs as shown in Fig. 3, it is denoted as SC-CNN₄. The loss function L_k for the k th block can be expressed as,

$$L_k = \sum_{e=1}^M (\varepsilon_{r,k'} - \varepsilon_{r,k})^2, \quad (13)$$

where $\varepsilon_{r,k'}$ and $\varepsilon_{r,k}$ denote the output and label of the k th block, respectively and M represents the total number of elements. The loss function of the SC-CNNs is composed of the cost functions in all blocks, which can be defined as follows,

$$L = \sum_{k=1}^N (\lambda_k \cdot L_k), \quad (14)$$

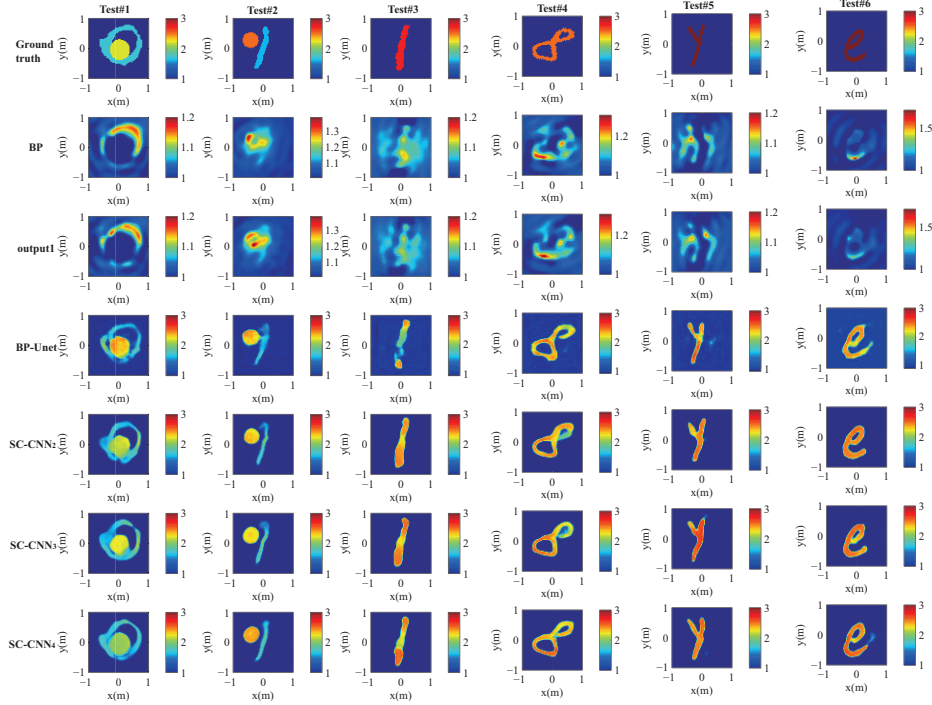


Fig. 5. The test results of example 1, 2 and 3 are shown here. Test#1 and Test#2 are example 1 with the relative permittivity between 1.5 to 2.5, Test#3 and Test#4 are example 2 with the relative permittivity between 2.5 to 3, Test#5 and Test#6 are example 3 with the relatively permittivity 3, output1 is the output of block1, which is similar to the results of BP.

TABLE I

The weight parameters of the loss function for each network (X means there is no such weight parameter)

	λ_1	λ_2	λ_3	λ_4
SC-CNN ₂	10/5/2	20	X	X
SC-CNN ₃	10/5/2	1	18	X
SC-CNN ₄	10/5/2	1	2	5

where λ_k is the weight coefficient of the cost functions at k th block. And all blocks are trained together by this loss function, every block is affected by the loss function on the blocks that follow it.

In the whole process of high-resolution imaging, the contribution of each block to the reconstruction results is different. The importance of each block can be effectively controlled by the weight parameters λ_k . To balance the loss function of each block, we try to keep the different loss functions of all blocks, i.e., $\lambda_1 * L_1, \lambda_2 * L_2, \dots, \lambda_n * L_n$, in the same order of magnitudes. Then, we maintain the weight of the first block unchanged. The weights of the remaining blocks, as well as the number of the blocks in the second part, could be adjusted according to the testing performance on the validating set. The training curve (red line) and validation curve (blue line) of SC-CNN₄ are shown in Fig. 4 (b), where they eventually converge in similar trends and magnitudes.

D. Computational Complexity

For the proposed SC-CNNs, the computational expense includes ReLU function, convolutions, batch normalization

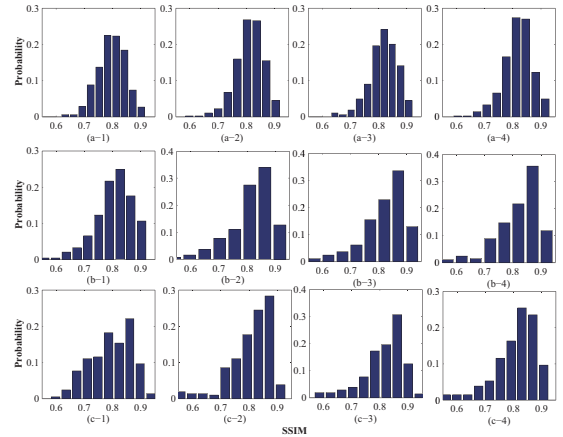


Fig. 6. Probability distribution of SSIM. (a-1) to (a-4) are BP-Unet, SC-CNN₂, SC-CNN₃, and SC-CNN₄ results of example 1, respectively. (b-1) to (b-4) are BP-Unet, SC-CNN₂, SC-CNN₃, and SC-CNN₄ results of example 2, respectively. (c-1) to (c-4) are BP-Unet, SC-CNN₂, SC-CNN₃, and SC-CNN₄ results of example 3, respectively.

TABLE II

The SSIM for BP-Unet, SC-CNNs of example 1, 2 and 3

	Example1	Example2	Example3
BP-Unet	0.7964	0.8060	0.7956
SC-CNN ₂	0.8118	0.8124	0.8082
SC-CNN ₃	0.8173	0.8184	0.8158
SC-CNN ₄	0.8339	0.8170	0.8225

and so on. The time-consuming cost one is the operations of convolutions. If there are Q_i input feature maps and Q_o output feature maps, the output feature map size is $N_1 \times N_2$ and the convolution kernel size is $K_f \times K_f$ ($K_f = 3$ and 5 in this paper, the size of the convolution kernel used in the convolution is 5×5 , and the size of the convolution kernel used in the up-convolution is 3×3). In the process of convolution, a slightly larger convolution kernel is used to extract more features.), thus the computational cost in the convolution layer is $O(N_1 N_2 K_f^2 Q_i Q_o)$ [34]. And in addition to that, there is the calculation of the BP, i.e., the label of block1, the computation cost is mainly composed of the calculation of the operator multiplication, i.e., $G_D(I)$ is the most complicated. The DoI D is discretized into $M = M_1 \times M_2$ pixels, if Fast Fourier Transformation (FFT) is applied in the matrix-vector multiplication, the computation cost is $O(N_f M \log M)$, where $M \log M$ is the computation cost of matrix-vector multiplication with FFT in each iteration of the forward solver, N_f denotes the number of the iterations of the forward problem.

IV. NUMERICAL SIMULATION

In this section, both the synthetical data and experimental data are presented to evaluate the proposed SC-CNNs in Section III. The BP-Unet in [24], is used to compared with the proposed method in terms of the inversion accuracy and the computational cost.

A. Numerical Setup

In the training process, MNIST data set is used for the training set [35]. It is composed of ten digits from 0 to 9 written by 250 different people and MNIST data set contains 70,000 images of handwritten digits. Herein, in order to increase the richness of the training data, a cylinder with random size and position is added into to the DoI with the profile from MNIST data set. Besides, in order to make the data set as diverse as possible, all samples are rotated arbitrarily from 0 to 360. The relative permittivity of the samples is set between 1.5 and 2.5, as shown in column 4 of Fig. 3. There are 10000 samples are generated according to the above requirements, of which 9000 ones are randomly selected for training, 500 samples are used for validation and the rest is for testing.

In the forward problem, we discretize a DoI D into 64×64 pixels with a size of $2 \text{ m} \times 2 \text{ m}$. 32 receiving antennas and 16 incident antennas are placed evenly around a circle with a radius of 3 m centered at (0, 0) m. The operating frequency is 400 MHz. And then MoM is implemented to get the scattered field data, e.g., \bar{E}^{sca} , with the size of $N_r \times N_i$, and there is no noise in the training data. To validate the robustness of the inversion methods, the test data is added white Gaussian noise \bar{n} and the noise is measured in terms of $(\|\bar{n}\| / \|\bar{E}^{sca}\|)$. For a more accurate evaluation of the inversion profiles, the structural similarity (SSIM) metric is used for the quantification. SSIM is a measure of the similarity for two images, and it goes from 0 to +1. When two images are exactly the same, it is equal to 1.

The hyperparameters for training procedure are set as follows: the Adam optimization algorithm is chosen to optimize

the proposed SC-CNNs, the exponential decay rate is set as $\beta_1 = 0.9$ and $\beta_2 = 0.99$; learning rate is gradually decreased, which is set as $1e-3$, $1e-4$, and $1e-5$, respectively, in the first 30 epochs, between 30 and 60 epochs, and after 60 epochs; batch size is set as 32, and the training is run with maximal 100 epochs. And the sever with Inter(R) Core(TM) i7-8700K CPU, 32G RAM, and GeForce GTX 2080Ti GPU is used for training and testing.

To investigate the numbers of Unet-CNN blocks needed in the second part, the SC-CNNs with two, three, four cascaded blocks are used in the training process, which are denoted as SC-CNN₂, SC-CNN₃, SC-CNN₄, respectively. Generally speaking, the more difficult the ISPs you solve, the more number of the blocks should be needed in the proposed SC-CNNs. The weight parameters of loss functions for each block in SC-CNN₂, SC-CNN₃, SC-CNN₄ are shown in Table I, respectively. The weight parameters set here remain the same for all examples, and they change only when the number of cascaded networks changes. In the SC-CNNs, block1 plays a significant role in the transformation from the scattered field to the images especially at the beginning of the training. So, the weight parameter λ_1 is gradually reduced, which follows the exact strategy: λ_1 is set as 10, 5, and 2 in the first 30 epochs, between 30 and 60 epochs, after 60 epochs. The loss curves of SC-CNN₂, SC-CNN₃, SC-CNN₄ for the training are depicted in Fig. 4 (a), it is shown that all of them have good convergence after 70 epochs. Also as seen from Fig. 4 (b), both the loss curves of the training set and validation set can keep stable after about 70 epochs.

B. Numerical Tests

In the example 1, the cascaded network is trained with SC-CNN₂, SC-CNN₃, SC-CNN₄ and BP-Unet, respectively. The MNIST data set with random cylinder (similar to the training set) is used for test and the relative permittivity is set between 1.5 and 2.5 with 20% added white Gaussian noises (AWGN) into the synthetical field data.

As depicted in Test#1 and Test#2 in Fig. 5, the reconstructed profiles obtained by these four methods are good and there are not much difference. The results by SC-CNNs methods are a little better than the one by BP-Unet. Whereas, the performance by increasing the number of cascaded networks is not significantly improved. In the following, the same training set in example 1 is used for example 2 and 3, but the relative permittivities of the tested samples are larger than the one in the training set. The profiles from MNIST data set and the Letter data set are selected for the test of the example 2 and 3. The Letter data set is composed of 26 handwritten letters of the English alphabet and contains a total of 2860 samples. In the example 2 and 3, the relative permittivities of the MNIST and the Letter are set as the one from 2.5 to 3 and 3, respectively. In the testing, both of the scattered field data is added with 5% AWGN. As known to all, when the relative permittivity of unknown targets increases, the nonlinearity of the model is also increased and the corresponding inversion become more and more difficulty compared to the example 1. The retrieval results are shown in Test#3-6 of Fig. 5.

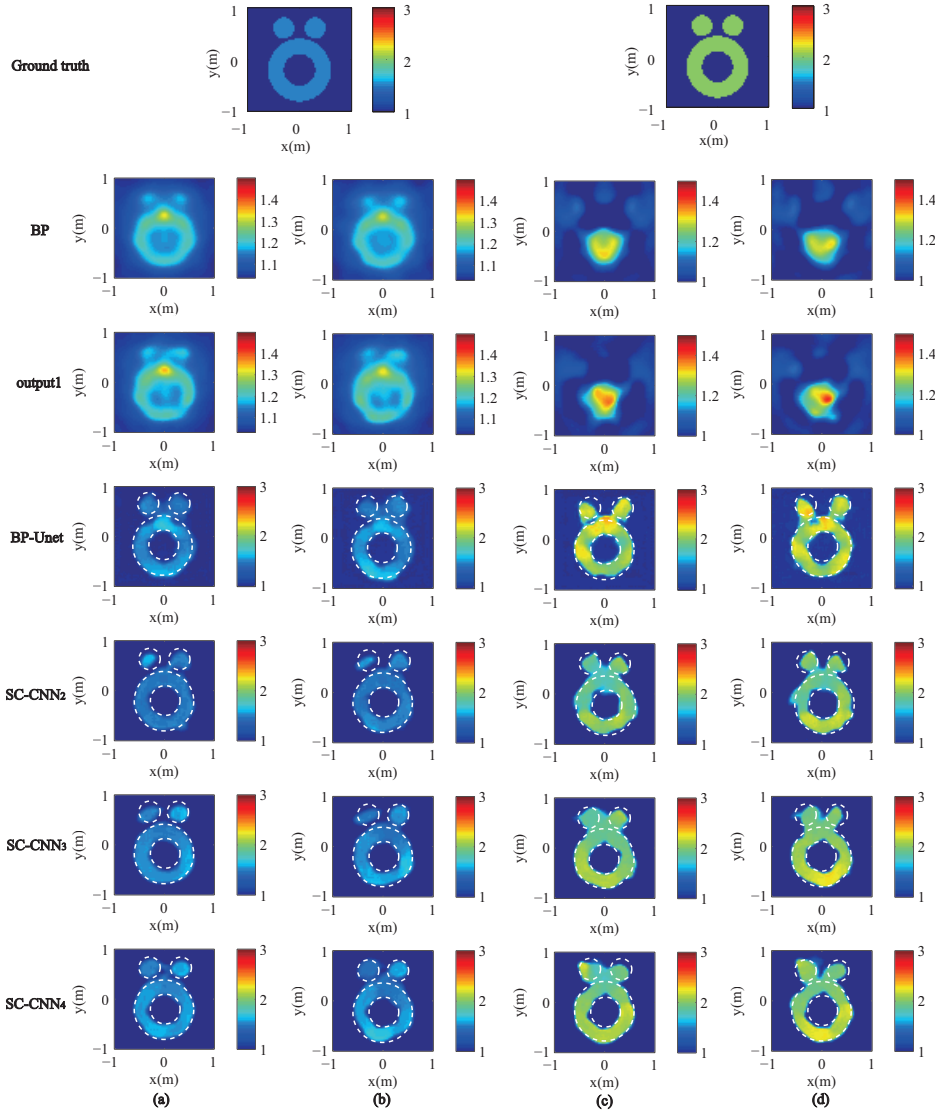


Fig. 7. Tests on “Austria” with the network trained by MNIST data set with a random cylinder. The ground truth in the first row, the relative permittivity on the left is smaller than that on the right. The added noise in the scattering field of (a) and (c) are 5%, while 20% Gaussian noise are presented in the scattered fields of (b) and (d).

It can be seen clearly, although the relative permittivities are larger than the one in example 1, the reconstructed results are still satisfactory. And the reconstructed results by the SC-CNNs are much better than BP-Unet. The average SSIMs for the reconstructed profiles by BP-Unet, SC-CNN₂, SC-CNN₃, SC-CNN₄ of example 1, 2, and 3 are shown in Table II. And the probability distribution of SSIM for the testing set are depicted in Fig. 6. Both of Fig. 6 and the statistical SSIM in Table II all validate that SC-CNNs inversion method can get better reconstruction accuracy compared to the BP-Unet. And more cascaded networks can improve the inversion performance if the nonlinearity of the solved ISPs is higher.

However, both the test examples with the profiles from MNIST and Letter data set are a little similar with the one in the training set. To further verify the generalization ability of the proposed methods, the benchmark testing profile, i.e., “Austria”, is tested in the example 4, which is much more challenging than the previously mentioned examples. In this

TABLE III
The SSIM for BP-Unet, SC-CNNs of “Austria” profile

	E4(a)	E4(b)	E4(c)	E4(d)
BP-Unet	0.7313	0.7046	0.6659	0.6817
SC-CNN ₂	0.7661	0.7358	0.7177	0.6886
SC-CNN ₃	0.7925	0.7616	0.7324	0.6952
SC-CNN ₄	0.8131	0.7737	0.7529	0.7192

example, the samples with the relative permittivities of 1.5 and 2 are utilized in Fig. 7 (a-b) and (c-d), respectively. And the scattered field data with AWGN of 5% and 20% is used to reconstruct the targets. When the relative permittivity of “Austria” profile is 1.5, it can be seen clearly from Fig. 7 (a) and (b) that the block1 mimicking the BP can well get the outline of the “Austria” profile and all the methods can successfully reconstruct the final targets. The results by the SC-

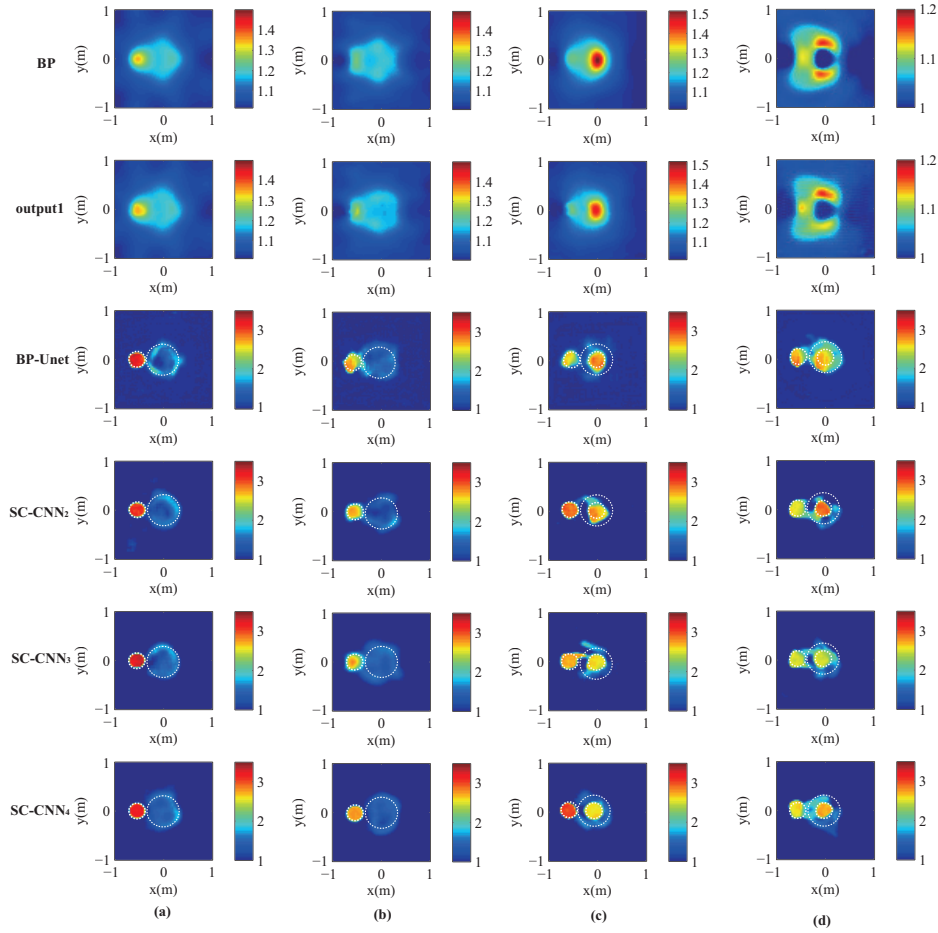


Fig. 9. Test on “*FoamDielExt*” and “*FoamTwinDiel*” profiles: reconstructed results at (a) and (c) 3GHz, (b) and (d) 4GHz.

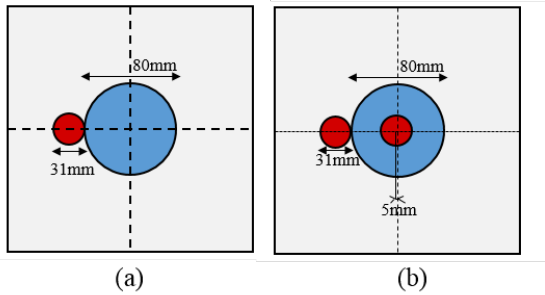


Fig. 8. (a) “*FoamDielExt*” profile and (b) “*FoamTwinDiel*” profile: the diameter of the red cylinder is 31 mm and the relative permittivity is 3 ± 0.3 . While the big cylinder has a diameter of 80 mm and the relative permittivity is 1.45 ± 0.15 .

CNNs are better than the one got by BP-Unet and are getting more and more better when the number of cascaded network is increased. As you can see from Fig. 7, the above two small circles are more clearer and the separation between the circles and the ring is more obvious. The quantitative results are summarized in Table III. From the retrieved profiles and the quantitative results, it is validated that the SC-CNN₄ achieves the best performance in terms of the inversion accuracy.

In the testing stage, with the trained network, the average

time for BP-Unet, SC-CNN₂, SC-CNN₃, SC-CNN₄ to test a sample is about 2s (obtaining BP results and network testing), 0.151s, 0.157s, 0.162s. It can be seen that testing time of SC-CNNs is shorter, and increasing the number of block2 in the second part has no obvious effect on the testing time.

C. Experimental Tests

In order to further demonstrate the effectiveness of the proposed method, the experimental tests are carried out against with the data from the Fresnel Institute [36].

As presented in Fig. 8, a “*FoamDielExt*” profile and a “*FoamTwinDiel*” profile with TM case are chosen to further test the performance of the proposed SC-CNNs. Different from the previous synthetic examples, 241 incident antennas and 8 receiving antennas are used in Fig. 8 (a), also 241 incident antennas and 18 receiving antennas are used in Fig. 8 (b) to collect the scattered field data at the working frequencies from 2 to 10 GHz with a step of 1 GHz. Accordingly, the size of DoI is also changed from $2.0 \text{ m} \times 2.0 \text{ m}$ to $0.2 \text{ m} \times 0.2 \text{ m}$. Detailed information about this experimental example can be found in [36]. The “*FoamDielExt*” profile contains two cylinders as shown in Fig. 8 (a), and the “*FoamTwinDiel*” profile is composed of three cylinders as shown in Fig. 8 (b). The diameter of the larger cylinder is 80 mm, and the relative

TABLE IV

The SSIM of “FoamDielExt” and “FoamTwinDiel” examples by BP-Unet and SC-CNNs corresponding to the Fig. 9 (a) - (d)

	(a)	(b)	(c)	(d)
BP-Unet	0.8330	0.8143	0.7965	0.7959
SC-CNN ₂	0.8343	0.8302	0.7975	0.7927
SC-CNN ₃	0.8440	0.8377	0.8055	0.8022
SC-CNN ₄	0.8782	0.8686	0.8245	0.8217

permittivity is 1.45 ± 0.15 . The diameter of the small cylinder is 31 mm, and the relative permittivity is 3 ± 0.3 . The null imaginary part of the profiles is omitted. In this example, the same MNIST profiles with random cylinders are taken as the training set as the above numerical examples. 9000 images from the MNIST set with random circles are used to train the model and the relative permittivity of them is randomly distributed between 1.5 and 3.3. In this experimental example, we change the frequency from 400 MHz to 3 and 4 GHz to be consistent with the experimental data.

Fig. 9 illustrates the reconstructed images when the operating frequency is 3 and 4 GHz. It can be seen that, both BP-Unet and SC-CNNs can obtain the satisfactory results at 3GHz. The average SSIMs of retrieval results for BP-Unet, SC-CNN₂, SC-CNN₃, and SC-CNN₄ are shown in Table IV. Consequently, the proposed SC-CNNs perform better than BP-Unet in terms of the profiles and the retrieval relative permittivities.

As the operating frequency is increased to 4 GHz, the nonlinearity of the model is improved accordingly. Compared to the results at 3 GHz, the overall reconstructed profiles look slightly worse, which are shown in Fig. 9 (b) and (d). The advantage of the SC-CNNs compared to BP-Unet are much more obvious from both the retrieval profiles and the quantitative results. Also, with increase of the number of cascading networks, the recovery of large cylinder is getting better. All above results validate that the superiority of the proposed SC-CNNs. And according to the difficulty of the problems you solved, more cascaded networks can be used to enhance the inversion performance .

V. CONCLUSION

In this paper, we have proposed an end-to-end scalable cascaded convolutional neural networks (SC-CNNs) to solve the ISPs with homogeneous background. As we know, black-box refers to the lack of clarity on the way the network learns mapping. Its uncertain how the input effectively approaches to the target through the network and what is the meaning of the hidden layers inside the network. To avoid the direct inversion scheme via a black-box way, the proposed SC-CNNs are composed of two parts, i.e., one CNN block for the linear transformation from the field data to the rough image and the other cascaded CNN blocks to enhance the resolution of reconstruction. The first block is used to mimic the BP procedure with the result of BP being taken as the label of the first network. And the second block is composed of several cascaded CNN blocks, which is utilized to fulfill the image-to-image transformation. In those cascaded CNN blocks, the

multi-scale labels with more and more high-frequency components are used to guide the cascaded network gradually to achieve the high-resolution imaging. Therefore, the SC-CNNs improve the physical meaning and interpretability in a progressive way. Both synthetic and experimental examples are implemented to validate the superior performance compared to DIS and the BP-Unet in terms of both the inversion accuracy and computational efficiency. Especially, for the moderate difficult example, such as “Austria”, “FoamDielExt” and “FoamTwinDiel” profiles, SC-CNNs can also obtain satisfactory results. Besides, according to the difficulties of the ISPs, the second part of the SC-CNNs can be scalable and we can add or reduce the corresponding blocks to obtain better results in an efficient and unified way.

REFERENCES

- [1] R. Chen, Z. Wei, and X. Chen, “Three dimensional through-wall imaging: Inverse scattering problems with an inhomogeneous background medium,” in *Proc. IEEE 4th AsiaPacific Conf. Antennas Propag. (APCAP)*, Jun./Jul. 2015, pp. 505506.
- [2] L.-P. Song, C. Yu, and Q. H. Liu, “Through-wall imaging (TWI) by radar: 2-D tomographic results and analyses,” *IEEE Trans. Geosci. Remote Sens.*, vol. 43, no. 12, pp. 27932798, 2005.
- [3] H. Kagiwada, R. Kalaba, S. Timko, and S. Ueno, “Associate memories for system identification: Inverse problems in remote sensing,” *Math. Comput. Model.*, vol. 14, pp. 200202, 1990.
- [4] A. Quarteroni, L. Formaggia, and A. Veneziani, *Complex Systems in biomedicine*. New York, Milan: Springer, 2006.
- [5] X. Wang, T. Qin, R. S. Witte, and H. Xin, “Computational feasibility study of contrast-enhanced thermoacoustic imaging for breast cancer detection using realistic numerical breast phantoms,” *IEEE Trans. Microw. Theory Techn.*, vol. 63, no. 5, pp. 1489-1501, 2015.
- [6] P. M. Meaney, M. W. Fanning, D. Li, S. P. Poplack, and K. D. Paulsen, “A clinical prototype for active microwave imaging of the breast,” *IEEE Trans. Microw. Theory Techn.*, vol. 48, no. 11, pp. 1841-1853, 2000.
- [7] X. Chen, “Subspace-based optimization method for solving inverse scattering problems,” *IEEE Trans. Geosci. Remote Sens.*, vol. 48, no. 1, pp. 4249, 2010.
- [8] Y. Zhong and X. Chen, “An FFT twofold subspace-based optimization method for solving electromagnetic inverse scattering problems,” *IEEE Trans. Antenna Propag.*, vol. 59, no. 3, pp. 914927, 2011.
- [9] K. Xu, Y. Zhong, and G. Wang, “A hybrid regularization technique for solving highly nonlinear inverse scattering problems,” *IEEE Trans. Microw. Theory Techn.*, vol. 66, no. 1, pp. 1121, 2018.
- [10] T. M. Habashy, M. L. Oristaglio, and A. T. de Hoop, “Simultaneous nonlinear reconstruction of two-dimensional permittivity and conductivity,” *Radio Sci.*, vol. 29, no. 4, pp. 11011118, 1994.
- [11] P. M. van den Berg, A. L. van Broekhoven, and A. Abubakar, “Extended contrast source inversion,” *Inverse Probl.*, vol. 15, no. 5, p. 1325, 1999.
- [12] P. M. van den Berg and R. E. Kleinman, “A contrast source inversion method,” *Inverse Probl.*, vol. 13, pp. 1607-1620, 1997.
- [13] F. Gao, B. D. Van Veen, and S. C. Hagness, “Sensitivity of the distorted born iterative method to the initial guess in microwave breast imaging,” *IEEE Trans. Antenna Propag.*, vol. 63, no. 8, pp. 3540-3547, 2015.
- [14] P. Mojabi and J. LoVetri, “Comparison of TE and TM inversions in the framework of the Gauss-Newton method,” *IEEE Trans. Antennas Propag.*, vol. 58, no. 4, pp. 1336-1348, 2010.
- [15] T. Rubaek, P. M. Meaney, P. Meincke, and K. D. Paulsen, “Nonlinear microwave imaging for breast-cancer screening using Gauss-Newton’s method and the CGLS inversion algorithm,” *IEEE Trans. Antenna Propag.*, vol. 55, no. 8, pp. 2320-2331, 2007.
- [16] T. M. Habashy, R. W. Groom, and B. R. Spies, “Beyond the Born and Rytov approximations: A nonlinear approach to electromagnetic scattering,” *J. Geophys. Research: Solid Earth*, vol. 98, no. B2, pp. 17591775, 1993.
- [17] K. Belkebir, P. C. Chaumet, and A. Sentenac, “Superresolution in total internal reflection tomography,” *J. Opt. Soc. Amer. A, Opt. Image Sci.*, vol. 22, no. 9, pp. 18891897, 2005.
- [18] K. Agarwal, X. Chen, and Y. Zhong, “A multipole-expansion based linear sampling method for solving inverse scattering problems,” *Opt. Express.*, no. 6, pp. 6366-6381, 2010.

- [19] K. Ito, B. Jin, and J. Zou, "A direct sampling method to an inverse medium scattering problem," *Inverse Probl.*, vol. 28, no. 2, p. 025003, 2012.
- [20] A. Massa, D. Marcantonio, X. Chen, M. Li, and M. Salucci, "DNNs as applied to electromagnetics, antennas, and propagation - A review," *IEEE Antennas Wireless Propag. Lett.*, vol. 18, no. 11, pp. 2225-2229, 2019.
- [21] X. Chen, Z. Wei, M. Li, and P. Rocca, "A review of deep learning approaches for inverse scattering problems (Invited Review)," *Prog. Electromagn. Res.*, vol. 167, pp. 67-81, 2020.
- [22] K. H. Jin, M. T. McCann, E. Froustey, and M. Unser, "Deep convolutional neural network for inverse problems in imaging," *IEEE Trans. Image Process.*, vol. 26, no. 9, pp. 45094522, 2017.
- [23] L. Li, L. Wang, F. Teixeira, C. Liu, A. Nehorai, and T. Cui, "DeepNIS: Deep neural network for nonlinear electromagnetic inverse scattering," *IEEE Trans. Antenna Propag.*, vol. 67, no. 3, pp. 1819-1825, 2018.
- [24] Z. Wei and X. Chen, "Deep-learning schemes for full-wave nonlinear inverse scattering problems," *IEEE Trans. Geosci. Remote Sens.*, vol. 57, no. 4, pp. 1849-1860, 2019.
- [25] L. Zhang, K. Xu, R. Song, X. Ye, G. Wang, and X. Chen, "Learning-based quantitative microwave imaging with a hybrid input scheme," *IEEE Sens. J.*, vol. 20, no. 24, pp. 15007-15013, 2020.
- [26] O. Ronneberger, P. Fischer, and T. Brox, "U-net: Convolutional networks for biomedical image segmentation," in *Proc. 18th Int. Conf. Med. Image Comput. Comput.-Assist. Intervent. (MICCAI)*, pp. 234-241, 2015.
- [27] R. Guo, X. Song, M. Li, F. Yang, S. Xu, and A. Abubakar, "Supervised descent learning technique for 2-D microwave imaging," *IEEE Trans. Antenna Propag.*, vol. 67, no. 5, pp. 3550-3554, 2019.
- [28] Y. Wang, L. Wang, H. Wang, and P. Li, "End-to-end image super-resolution via deep and shallow convolutional networks," *IEEE Access*, vol. 7, pp. 31959-31970, 2019.
- [29] H. Yao, W. E. I. Sha, and L. Jiang, "Two-step enhanced deep learning approach for electromagnetic inverse scattering problems," *IEEE Antennas Wireless Propag. Lett.*, vol. 18, no. 11, pp. 2254-2258, 2019.
- [30] Z. Wei and X. Chen, "Physics-inspired convolutional neural network for solving full-wave inverse scattering problems," *IEEE Trans. Antenna and Propag.*, vol. 67, no. 9, pp. 6138-6148, 2019.
- [31] X. Chen, *Computational Methods for Electromagnetic Inverse Scattering*. Hoboken, NJ, USA: Wiley, 2018.
- [32] A. F. Peterson, S. L. Ray, and R. Mittra, *Computational Methods for Electromagnetics*. Hoboken, NJ, USA: Wiley, 1998.
- [33] S. Ioffe and C. Szegedy, "Batch normalization: Accelerating deep network training by reducing internal covariate shift," *Proc. Int. Conf. Mach. Learn.*, 2015, pp. 448-456.
- [34] J. Cong and B. Xiao, "Minimizing computation in convolutional neural networks," in *Proc. 24th Int. Conf. Artif. Neural Netw.*, 2014, pp. 281-290.
- [35] Y. LeCun, L. Bottou, Y. Bengio, and P. Haffner, "Gradient-based learning applied to document recognition," *Proc. IEEE*, vol. 86, no. 11, pp. 2278-2324, 1998.
- [36] J.-M. Geffrin, P. Sabouroux, and C. Eyraud, "Free space experimental scattering database continuation: Experimental set-up and measurement precision," *Inverse Probl.*, vol. 21, no. 7, pp. 117-130, 2005.



Kuiwen Xu received the B.E. degree from Hangzhou Dianzi University, and the Ph.D. degree from Zhejiang University, Hangzhou, China, in 2009 and 2014, respectively.

From 2012 to 2013, he was a Visiting Ph.D. Student with the National University of Singapore, Singapore. From 2014 to 2015, he was a Senior Researcher with Huawei Technologies Company, Ltd., Hangzhou. He was invited to the State Key Laboratory of Terahertz and Millimeter Waves, City University of Hong Kong, Hong Kong, as a Visiting

Professor, in 2018. Since September 2015, he has been with Hangzhou Dianzi University, Hangzhou, where he is currently a Professor. He has published 50 journal articles on electromagnetics inverse problems, antenna design and synthesis, microwave measurement and sensing. His research interests include computational imaging and electromagnetics inverse problems, machine learning-based wireless sensing and imaging, and new concept antennas (5G MIMO antenna, Meta-antenna, etc.).



Cheng Zhang received the B.E. degree from Qingdao University of Science and Technology, Qingdao, China, in 2019. She is currently pursuing the M.S. degree in Hangzhou Dianzi University. Her current research interests include microwave imaging and electromagnetic inverse scattering problems.



Xiuzhu Ye received the B.E. degree in Telecommunication Engineering from Harbin Institute of Technology, Harbin, China, in 2008 and the Ph.D. degree from Department of Electrical and Computer Engineering in National University of Singapore, Singapore, in 2012.

From 2012 to 2013, she worked in Department of Electrical and Computer Engineering, National University of Singapore as a Research Fellow. Since 2013, she worked as Assistant Professor in Beihang University. Since 2019, she has been an Associate

Professor with School of Information and Electronics, Beijing Institute of Technology. Her research areas are electromagnetic inverse problems, microwave imaging methods, antenna designing and machine learning. Dr. Ye has served on review boards of various technical journals, including IEEE Transactions on Antenna and Propagation, IEEE Transactions on Microwave Theory and Techniques, Radio Science and Optics Express.



Rencheng Song received his B.S. degrees from Jilin University, Changchun, China, in 2005, and the Ph.D. degree from Zhejiang University, Hangzhou, China in 2010, both in computational mathematics. From 2010 to 2012, he was a Research Fellow with the National University of Singapore, Singapore. From 2013 to 2017, he was a Principal Scientist with Halliburton Far East Pte Ltd, Singapore. Since May 2017, he has been with the Department of Biomedical Engineering at Hefei University of Technology, Hefei, China, as an associate professor. His research

interests include intelligent perceptions for biomedical measurements, such as electromagnetic imaging, video-based physiological parameter measurement, and machine learning.